A Computational Study of Equivalence Ratio Effects in Turbulent, Premixed Methane-Air Flames

John B. Bell, Marcus S. Day, Joseph F. Grcar, and Michael J. Lijewski

Center for Computational Science and Engineering, Lawrence Berkeley National Laboratory, Berkeley, CA 94720, USA

Abstract

In this paper we present numerical simulations of two-dimensional turbulent methane combustion using GRI-Mech 3.0 at equivalence ratios $\phi = 0.55$ and $\phi = 1.00$. The simulations are performed using a low Mach number adaptive mesh refinement algorithm coupled to an automatic feedback control algorithm that stabilizes the flame on the computational grid. We present probability density functions for curvature, strain and a local flame speed based on fuel-consumption. We also present joint probability density functions showing correlations of the local flame speed with curvature and showing that the local flame speed does not correlate with the tangential strain rate evaluated in the cool part of the flame. The simulation data is indicative of a change in Markstein number as we change equivalence ratio with the lean flame being thermo-diffusively unstable. We introduce a pathline diagnostic that allows us to computationally follow parcels of fluid through the flame and quantify the associated reaction and diffusive transport processes. Using this diagnostic, we examine the differences in the chemical and transport properties of the two flames that lead to the shift in Markstein number.

Keywords: turbulent premixed combustion, low Mach number flow, adaptive mesh refinement

1. Introduction

In an earlier paper [1], we introduced an automatic control algorithm that can be used to computationally stabilize a premixed turbulent flame in a simple channel configuration in which a laminar premixed flame is domain and allowed to propagate into a turbulent inflow. A simple feedback control algorithm is employed to dynamically adjust the mean inflow rate at this boundary to stabilize the mean flame position in the domain. In this paper, we consider the simulation of methane flames at two equivalence ratios, examining in detail the statistics of local flame speed, curvature and tangential strain rate. We also look in detail at the chemical and transport behavior of the flames to categorize how the flame dynamics shifts with changes in equivalence ratio.

There is an extensive literature on computational studies of this type in 2D and 3D without feedback control, both with simplified and detailed chemistry. See the references in [1] for a detailed review of the literature. In the next section, we briefly discuss our computational approach and the two simulation cases we consider. The following section introduces a diagnostic procedure we will use to analyze the simulation data. Computational results are discussed in the final section.

2. Computational model

The simulation is based on a low-Mach-number formulation in which the background thermodynamic pressure remains constant. The methodology treats the fluid as a mixture of perfect gases, and uses a mixture-averaged model for differential species diffusion, ignoring Soret, Dufour and radiation effects. With these assumptions, the equations governing the flow are given by

$$\frac{\partial \rho U}{\partial t} + \nabla \cdot \rho UU = -\nabla \pi + \nabla \cdot \tau, \tag{1}$$

$$\frac{\partial \rho Y_m}{\partial t} + \nabla \cdot U \rho Y_m = \nabla \cdot \rho D_m \nabla Y_m + \rho \dot{\omega}_m, \tag{2}$$

$$\frac{\partial \rho h}{\partial t} + \nabla \cdot U \rho h = \nabla \cdot \frac{\lambda}{c_p} \nabla h + \tag{3}$$

$$+ \sum_m \nabla \cdot h_m \left(\rho D_m - \frac{\lambda}{c_p} \right) \nabla Y_m,$$

where ρ is the density, U is the velocity, Y_m is the mass fraction of species m, h is the mass-weighted enthalpy of the gas mixture, T is the temperature, and $\dot{\omega}_m$ is the net creation rate for specie m due to chemical reactions. Also, λ is the thermal conductivity, τ is the stress tensor, c_p is the specific heat of the mixture, $h_m(T)$ and D_m are the enthalpy and species mixture-averaged diffusion coefficients of species m, respectively. These evolution equations are supplemented by an equation of state for a perfect gas mixture:

$$p_0 = \rho R_{mix} T = \rho \mathcal{R} T \sum_m \frac{Y_m}{W_m} \tag{4}$$

where W_m is the molecular weight of species m, and $\mathcal{R}$ is the universal gas constant.

Our basic discretization algorithm combines a symmetric operator-split treatment of chemistry and diffusion processes with a density-weighted approximate projection method for incorporating the a velocity divergence constraint that enforces the equation of state constraint. This basic integration scheme is embedded in a parallel adaptive mesh refinement (AMR) algorithm. The adaptive algorithm is second-order accurate in space and time, and discretely conserves species mass and enthalpy. No explicit model for turbulence or turbulence / chemistry interaction is included. The reader is referred to [2] for details of the low-Mach-number model and its numerical implementation and to [3–5] for applications of this methodology to the simulation of premixed turbulent flames.

The flow configuration we consider initializes a flat laminar flame in a domain oriented so that the flame propagates downward. A cold fuel-air premixture enters the domain through bottom boundary, and hot combustion products exit the domain through the top. The remaining computational boundary is periodic. Along the inflow face we specify both a mean inflow velocity and turbulent fluctuations (discussed in more detail below) that are superimposed on the mean inflow. A control algorithm, introduced in Bell et al. [1], automatically adjusts the mean inflow rate to hold the flame at a fixed location in the domain. (See [1] for additional details.)

We apply the control methodology described above to two methane flames modeled using the GRI-Mech 3.0 chemistry mechanism (53 species, 325 reactions) and the associated mixture-averaged diffusive transport model. The flames are chosen to highlight variations observed in a methane flame's response to flow-field strain and flame surface curvature (see, for example, Tseng et al. [6]). In particular, we consider equivalence ratios of $\phi = 0.55$ and 1.0. Table 1 lists various properties of the corresponding steady laminar one-dimensional flame solutions computed using the PREMIX [7] code. The computational domains have dimensions $L \times H = 46\,\delta_L \times 92\,\delta_L$. The fluctuations in the inflow stream were generated for each case separately by generating a random vorticity field spectrally shaped to corresponding to two-dimensional turbulence. This random field is then evolved in time with an incompressible Navier Stokes solver to ensure proper phasing of the resulting velocity field. The resulting fluctuations have an effective integral scale length $\ell_t \sim 2.6\delta_L$ and turbulent intensity $u' \sim 1.7 s_L$, measured with respect to the the thermal thickness, δ_L and laminar burning speed, s_L, of each flame. These turbulent fluctuations are then added to the mean inflow velocity determined by the control algorithm

Adaptive mesh refinement was used to maintain approximately 44 uniform grid cells across the thermal width of the flames throughout their evolution. Dynamic refinement for these simulations was based

on the magnitude of vorticity and on a flame marker, CH_3. For both case, we waited until the flame height stabilized before collecting data for analysis.

3. Pathline analysis

We want to be able to analyze in detail the transport and chemical properties of the simulated flames. As a means to quantifying these effects, we identify an "infinitesimally small" parcel of the fluid and follow it as it passes into the flame zone, reacts and is then transported into the products. As we follow this parcel of fluid we can decompose the changes in its composition into two effects: changes due to reaction and changes due to transport. To express this mathematically, we write the species transport equations in Lagrangian form

$$\rho \frac{DY_m}{Dt} = \nabla \cdot \rho D_m \nabla Y_m + \rho \dot{\omega}_m, \qquad (5)$$

This equation express the change in Y_m with time along integral curves of the velocity; i.e., curves given by

$$\frac{dx}{dt} = v(x,t) \quad , \qquad (6)$$

commonly referred to as pathlines. In the Lagrangian frame the continuity equation reduces to $D\rho/Dt = 0$ so that, as the parcel of fluid is transported, the net mass in the parcel remains the same. The change in density along the pathline thus represents not a change in the mass of the parcel but rather a change in the volume that the parcel occupies.

Along this path the composition of the mixture can be changed by two effects: diffusion ($\nabla \cdot \rho D_m \nabla Y_m$) and reaction ($\dot{\omega}_m$). Our goal then is to separate these different effects. Before discussing how this can be done, it is useful to consider the choice of units for the analysis. There are several possibilities that can be considered; here we have chosen to use $Y_m/W_m \equiv [X_m]/\rho$ where W_m is the molecular weight of species m, which expresses the moles per unit mass in the parcel. This provides a natural way of representing the molar composition of the mixture so that changes in the volume of the mixture do not change the representation. For example if there is no species transport or chemical reaction in the system then Y_m/W_m will remain unchanged along the pathline.

The basic idea here then is to follow selected pathlines in the flow that represent parcels of fluid, monitoring changes in composition of the parcel and the volume it occupies. The change in composition can then be further decomposed into the changes caused by reaction and the changes caused by species transport. Our goal is to use this analysis procedure as a post-processing tool that can be used to interrogate simulation data.

Given a time sequence of snapshots of the evolving simulation, it is easy to construct a pathline by interpolating the velocity field from the simulations in space and time and integrating Eqn. 6. A similar type of interpolation procedure allows us to extract the composition of the mixture along the pathline. We used bilinear interpolation in space and linear interpolation in time to construct both the velocity field and the mixture composition between time snapshots. We characterized the mixture in term of its temperature and mole fractions; other quantities can be derived from these using standard thermodynamic operations. (Here, p is fixed as a consequence of the low Mach number model; in a more general case one additional thermodynamic variable is needed.)

The decomposition of the change in composition into reaction and transport components is somewhat more problematic. If the simulation data is stored a sufficiently fine temporal resolution, viz., at time increments in which the chemical kinetics can be accurately captured with simple singe-step temporal integration strategies then a straightforward evaluation of the rates along the path provides an adequate characterization of the reaction rates and the diffusive transport can be obtained from conservation considerations.

However, in our case with the larger time step allowed by the low Mach number model, the chemical kinetics are stiff on the time scale of the solution algorithm. (Chemistry is treated with a stiff ODE package in our simulation methodology.) When the chemical time scales are much shorter than the temporal increments between archived simulation data, a simple evaluation of the chemical rates leads to an inaccurate separation of chemistry and transport along the pathline.

To circumvent this difficulty, we observe that the chemistry occurring within the parcel is completely local. The only interaction a given parcel has with the surrounding fluid is through diffusive transport. We can use this property to construct an inverse problem whose solution will provide a decomposition of the right hand side of Eqn. 5. In particular, given (ρ_1, T_1, Y_m^1) and (ρ_2, T_2, Y_m^2) at the beginning and end of a time interval $[t_1, t_2]$, respectively we find an unknown diffusional source, $\mathcal{D}$, such that

$$\frac{DY_m}{Dt} = \rho \dot{\omega}_m + \frac{\mathcal{D}}{\rho}$$

with $Y_m(t_1) = Y_m^1$ and $Y_m(t_2) = Y_m^2$. For this construction, we discretize the path in small increments and assume that we can approximate $\mathcal{D}$ by a constant for each species on each interval. Furthermore, we assume that density and enthalpy vary linearly in time along the path. These assumptions require that we are sampling the data at a resolution on which the fluid dynamical behavior is smooth although the chemical behavior may not be. A simple Picard iteration is used to solve the problem.

4. Results

The focus of the first part of our analysis is on the dependence of the local fuel consumtion on curvature

and stretch strain. Figure **??** depicts the local fuel consumption in a sub-region of the domain for each equivalence ratio. For the $\phi = 0.55$ flame, the fuel consumption is enhanced in regions that are convex with respect to products and is reduced in cusps that are convex with respect to reactants. (We will define curvature so that these regions correspond to positive and negative curvature, respectively.) The situation for the stoichiometric flame is reversed with stronger burning near the cusps. This dependence on equivalence ratio is in agreement with experimental and computational evidence for premixed methane flames at atmospheric pressure. See, for example, [6, 8, 9].

To obtain a more quantitative characterization of this dependence, we construct a local flame speed based on integrated local fuel consumption. We first identify the flame with the isotherm at which fuel consumption reaches its maximum in the corresponding flat unstretched laminar flame (Table 1). We then define a local coordinate system near the flame using arc length along the flame and a normal coordinate defined in terms of temperature scaled to define a progress variable, c, such that $c = 0$ in the unburned reactants, and $c = 1$ in the products. At uniform intervals along the flame, we follow integral curves of the gradient of c toward both the products and fuel, defining a series of adjacent disjoint wedge-shaped volumes, Ω_k, surrounding the flame, and extending well beyond the region of high chemical reactivity. A local burning speed may then be defined over each of these volumes:

$$S_c^\ell = \frac{1}{A^\ell \left(\rho Y_{\text{Fuel}}\right)_{\text{in}}} \int_{\Omega_k} \rho \omega_{\text{Fuel}} d\Omega_k \qquad (7)$$

where A^ℓ is the area (length) of the intersection of Ω_k with the flame. For additional detail about these constructions see [1]. Classical flame theory treats the flame as a discontinuous interface propagating through the fluid (see, for example, Peters [10]). Interpreting this theory in the context of resolved flames is problematic, particularly with respect to defining strain. (A number of authors have proposed thick flame modifications to the classical theory, see for example, Chung and Law [11] and de Goey and coworkers [12–14].) As the fluid enters the preheat zone, the fluid begins to accelerate. Thus, the choice of where to evaluate the strain becomes an issue. If the flame is defined as the isotherm of peak heat release, then expansion through the flame induces a strong correlation between curvature and strain as observed by Pope [15] and by Haworth and Poinsot [16]. An alternative, which we have adopted here, is to evaluate the strain at a relatively low temperature. In particular, we have followed the integral curves of the progress variable until we reach the $T = 400$ K isotherm and evaluated the tangential strain rate there. This construction avoids flame acceleration effects but leads to other anomalies in highly cusped regions.
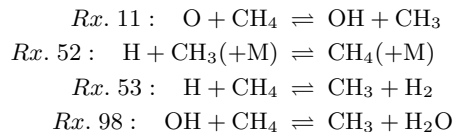
In Fig. 2 we show joint PDFs of local consumption flame speed versus curvature and strain. The data shows clear correlations between local flame speed and curvature. For the $\phi = 0.55$ flame this correlation is positive with enhanced speeds in regions of positive curvature indicating that the flame is thermodiffusively unstable. For the $\phi = 1.00$ flame the situation is reversed with negative curvature regions burning most strongly. We note that some of the high local speeds near zero curvature represent a breakdown in the construction of the integration regions Ω_k as long fingers of fuel extending into the products burn out. These regions also produce artifacts in the strain rate / flame speed joint PDF which can be seen in Fig. 2b,d as vertical striations. Finally, the joint PDF of cold tangential strain rate and local flame speed shows essentially no correlation — indicating that, for these flames, strain does not have a consistent local effect on the flame. A similar observation was made by Haworth and Poinsot [16] for single step chemistry.

In the remainder of this section, we use pathline analysis to examine how differences in chemistry and transport between the two flames lead to the changes in the response of the flames to curvature. To analyze this behavior, we construct two pathlines for each flame. In each case, one of the pathlines passes through a cusp and another passes through a the flame in a region of positive curvature which we will refer to as a "nose." The trajectories of the pathlines are shown in Figure 1. We emphasize that the pathlines are curves in space-time, but to view them, we have drawn their entire spatial migration on top of the snapshot of the flame at the one specific time that they cross the flame in the figure. Consequently, although it appears that the pathlines crosses the flame at an earlier time, this is simply an artifact of the picture; at the earlier time the flame was located elsewhere.

In Figure 3 we show the temperature and key components of the molar composition of the fluid parcels for each pathline as a function of time. For these plots and the others in this section, we have shifted the time scale so that $t = 0$ corresponds to the time of maximum heat release for that parcel of fluid. For comparison, we have also constructed a pathline for a flat laminar flame and plotted data for it as well. We note that in both cases, the temperature and methane temporal profiles are considerably smoother at the noses than at the cusps with the laminar flame being intermediate to the other two. In addition, we note that although the temperature profiles are smoother at the noses, the temperature at peak heat release is essentially the same as at the cusps.

If we examine the chemical behavior along the pathlines, we find that there are four reactions that play a key role in the direct oxidation of the methane

$$
\begin{aligned}
Rx.\ 11: \quad & O + CH_4 \rightleftharpoons OH + CH_3 \\
Rx.\ 52: \quad & H + CH_3(+M) \rightleftharpoons CH_4(+M) \\
Rx.\ 53: \quad & H + CH_4 \rightleftharpoons CH_3 + H_2 \\
Rx.\ 98: \quad & OH + CH_4 \rightleftharpoons CH_3 + H_2O
\end{aligned}
$$

(The reaction number correspond to their number in the GRI-3.0 reaction mechanism specification.) Thus,

the radicals, H, O, and OH are the key reaction partners that control the destruction of CH_4. These three radical are plotted, with enhanced vertical scales, in Figure ??. These graphs reveal some differences between the response of the two flames at cusps and noses. The radical profiles peak after the methane has been consumed and after the peak heat release. For the rich flame, we see that the peak concentration of the radical is higher in the cusps than in the nose. In addition, we note that the most prevalent radical is OH with H reaching almost the same level. The O radical concentration is substantially smaller than the other two. For the lean flame, we see two major differences. First, the higher peak concentration for each radical occurs in the nose not the cusp. In addition, although OH remains the most plentiful radical, the concentration of H is now substantially reduced while the relative amount of O has increased.

The effect of these differences on the reaction profiles is shown in Figure 4. Here we plot the net reaction rate for each of the reactions mentioned above as a function of time for each flame, with the convention that positive values refer to the production of methane. Thus, in each case, Rx. 11, 53, and 98 are always net methane destructors while Rx. 52 creates methane. Figure 4 shows that for both $\phi = 0.55$ and $\phi = 1.00$, the reactions profiles in the nose are broader than the reactions in the cusp, again reflecting the notion that in a Lagrangian sense, the passage of fluid through the noses occurs on a slower time scale than through the cusps. However, in the $\phi = 1.00$ case, the reactions at the cusp reach higher intensities than those at the nose while for $\phi = 0.55$ the reactions in the nose are not only of longer duration but also reach higher intensities. The relative intensification of these key reactions reflects the difference in behavior of the different equivalence ratios at noses and cusps.

Another difference between the two cases is the relative importance of the different reactions. For $\phi = 1.00$, Rx.'s 53 and 98 are essentially of equal importance with Rx.'s 11 and 52 playing a considerably less important role. For the lean case, Rx. 53 is dramatically reduced in magnitude with Rx. 98 playing the dominant role in the destruction of methane.

From this analysis, it is clear that the differences in the behavior of the radicals H, OH and O is a key determining factor to explain the shift in behavior of methane flames with equivalence ratio. To quantify the details of these radicals in more detail, in Figure 5, we show for each of them and for methane, a blowup showing the diffusive transport and reaction along the pathlines. We see that in both cases, the diffusion of methane out of the preheat zone is enhanced in the cusps, which represents a defocusing associated with transport of methane to nearby flame segments that provide a sink for methane. For the lean case, this loss of fuel is reflected in each of the radicals and results in a overall reduction in the intensity of the methane oxidation.

For the $\phi = 1.00$ case the situation is somewhat different. Here, the peak production of H in the nose and the cusp are comparable are as is the subsequent transport of H out of that region. However, on the cooler side of the flame we see a dramatic increase in the diffusive flux of H into the flame. (A similar effect is also seen in O but less severe.) This represents a diffusive focussing of highly mobile H radicals from nearby flame segments into this parcel of fluid. This enhancement in available H more than compensates for the loss of methane to diffusion in the preheat side of the flame and, in fact, the increased intensity of the reactions leads to more intense production of the other radicals as well. On the other hand, defocusing of O and OH at the nose overwhelms the focusing of methane into the region and a net reduction in methane destruction occurs.

Thus, the key difference between the response lean and stoichiometric flames to curvature can be traced to the relative composition of the radical pool. In particular, as the flame becomes lean, the excess oxygen in the system reduces the relative fraction of H in the radical pool. It is this H that is diffusively focussed onto parcels of fluid passing through cusps that leads to the vigor of reactions in the cusps for the stoichiometric flame.

5. Conclusions

In this paper we have presented numerical simulations of two-dimensional turbulent methane combustion using GRI-Mech 3.0 at equivalence ratios $\phi = 0.55$ and $\phi = 1.00$. In agreement with experimental data, the Markstein number based on a local fuel-consumption flame speed changes sign with the change in equivalence ratio. The simulation data shows that the local flame speed is well correlated with the curvature but is basically uncorrelated with the cold tangential strain rate. We have introduced a pathline diagnostic that allows us to computationally follow parcels of fluid through the flame and quantify the associated reaction and diffusive transport processes. Using this diagnostic, we have shown that for the lean case defocusing of the fuel leads to a reduction in the combustion intensity at cusps while for the $\phi = 1.00$ flame an intense focussing of radicals, particulary H, into the fluid enhances the combustion process and more than compensates for losses of methane to diffusion.

References

[1] J. B. Bell, M. S. Day, J. F. Grcar, M. J. Lijewski, *Comm. Appl. Math. Comput. Sci.* to appear.

[2] M. S. Day, J. B. Bell, *Combust. Theory Modelling* 4 (2000) 535–556.

[3] J. B. Bell, M. S. Day, I. G. Shepherd, M. Johnson, R. K. Cheng, J. F. Grcar, V. E. Beckner, M. J. Lijewski, *Proc. Natl. Acad. Sci. USA* 102 (29) (2005) 10006–10011.

[4] J. B. Bell, M. S. Day, J. F. Grcar, *Proc. Combust. Inst.* 29 (2002) 1987–1993.

[5] J. B. Bell, M. S. Day, J. F. Grcar, M. J. Lijewski, J. F. Driscoll, S. A. Filatyev, *Proc. Combust. Inst.* 31, submitted.

[6] L.-K. Tseng, M. A. Ismail, G. M. Faeth, *Combust. Flame* 95 (1993) 410–425.

[7] R. J. Kee, J. F. Grcar, M. D. Smooke, J. A. Miller, *PREMIX: A Fortran Program for Modeling Steady, Laminar, One-Dimensional Premixed Flames*, Technical Report SAND85-8240, Sandia National Laboratories, Livermore (1983).

[8] D. Bradley, P. H. Gaskell, X. J. Gu, *Combust. Flame* 104 (1996) 176–198.

[9] J. H. Chen, H. Im, *Proc. Combust. Inst.* 27 (1998) 819–826.

[10] N. Peters, *Turbulent Combustion*, Cambridge University Press, Cambridge, 2000.

[11] S. H. Chung, C. K. Law, *Combust. Flame* 72 (1988) 325–336.

[12] L. P. H. d. Goey, J. H. M. ten Thije Boonkkamp, *Combustion Science and Technology* 122 (1997) 399–405.

[13] L. P. H. d. Goey, R. M. M. Mallens, J. H. M. ten Thije Boonkkamp, *Combust. Flame* 110 (1997) 54–66.

[14] L. P. H. d. Goey, J. H. M. ten Thije Boonkkamp, *Combust. Flame* 119 (1999) 253–271.

[15] S. B. Pope, *Int. J. Engng. Sci.* 26 (1988) 445–469.

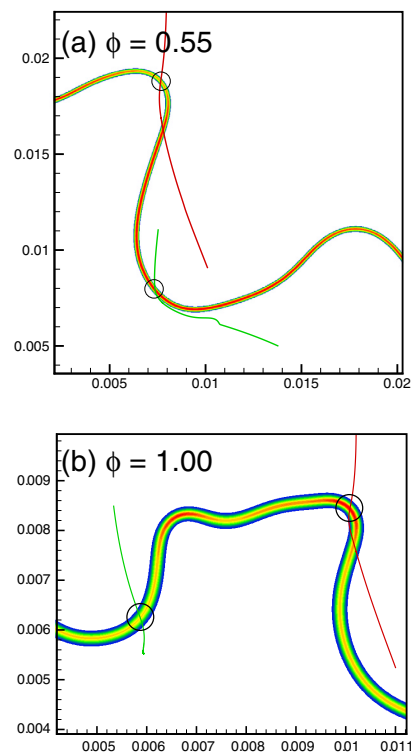[16] D. C. Haworth, T. J. Poinsot, *J. Fluid Mech.* 244 (1992) 405–436.

Fig. 1: Detail of methane consumption rate for (a) $\phi = 0.55$, and (b) $\phi = 1.00$ in subregion near diagnostic pathlines, indicating opposite correlations with flame surface curvature. Green pathlines pass through the respective flame surface at the instant of this time snapshot through a "nose" region, red pathlines pass through "cusps".
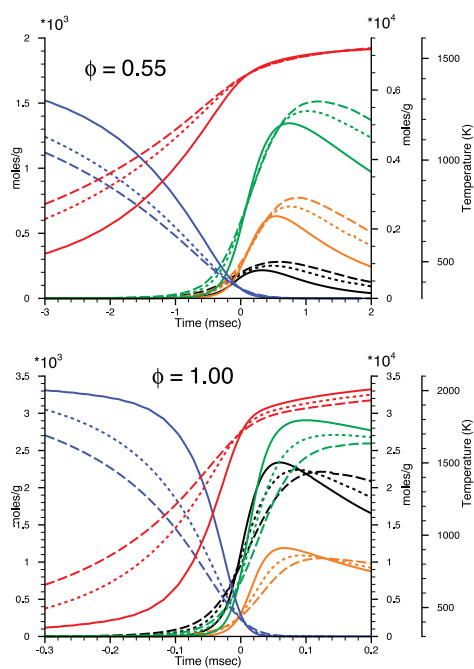
Fig. 3: Profiles of T (red), CH_4 (blue), H (black), OH (green) and O (orange) along the pathlines. Here the solid lines are the cusps, the long dashes are the noses and the short dashes are the laminar flame.
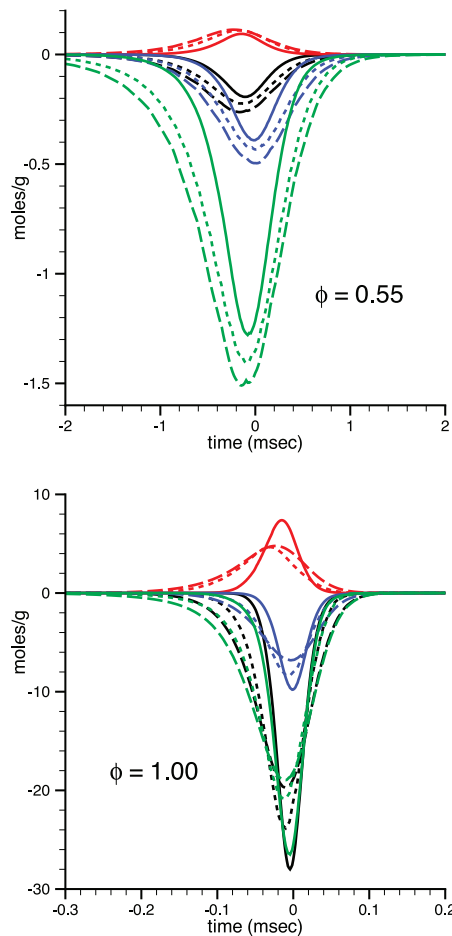

Fig. 4: Profiles of the key reactions along the pathlines. Here, Rx. 11 is blue, Rx. 52 is red, Rx. 53 is black and Rx. 98 is green. The solid lines are the cusps, the long dashes are the noses and the short dashes are the laminar flame.

Table 1: *Characteristics of the laminar methane-air flames of different stoichiometries at 1 atmosphere. Thermal flame thickness is calculated as the change in temperature through the flame divided by the maximum temperature gradient, $\delta_L = (T_{max} - T_{min})/\max \|\nabla T\|$.*

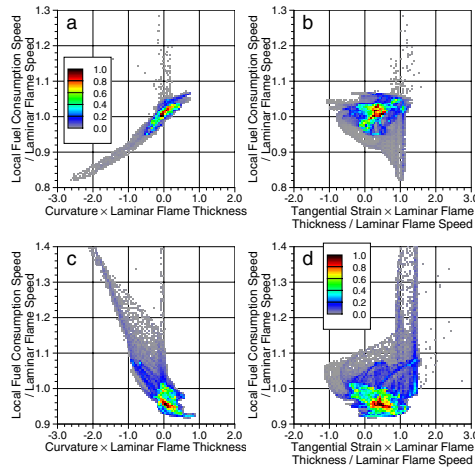| fuel equiv-alence ratio ϕ	thermal flame thickness δ_L (μm)	flame speed s_L (cm / s)	fuel consum-ption rate (g / cm s)	isotherm of peak heat release (K)	peak local fuel consumption (mg / mL s)
0.55	1313	7.62	0.0273	1379	7.03
1.00	433	36.2	0.2380	1684	134

Fig. 2: Joint probability density functions (JPDF's) of three nondimensionalized quantities: fuel consumption speed, curvature, and tangential strain. Coloration indicates density. In all figures, the greatest density lies in the small regions colored yellow, red, and black. The very large areas colored grey and blue account for just 20% of the probability distribution — the same as the very small areas colored red and black.
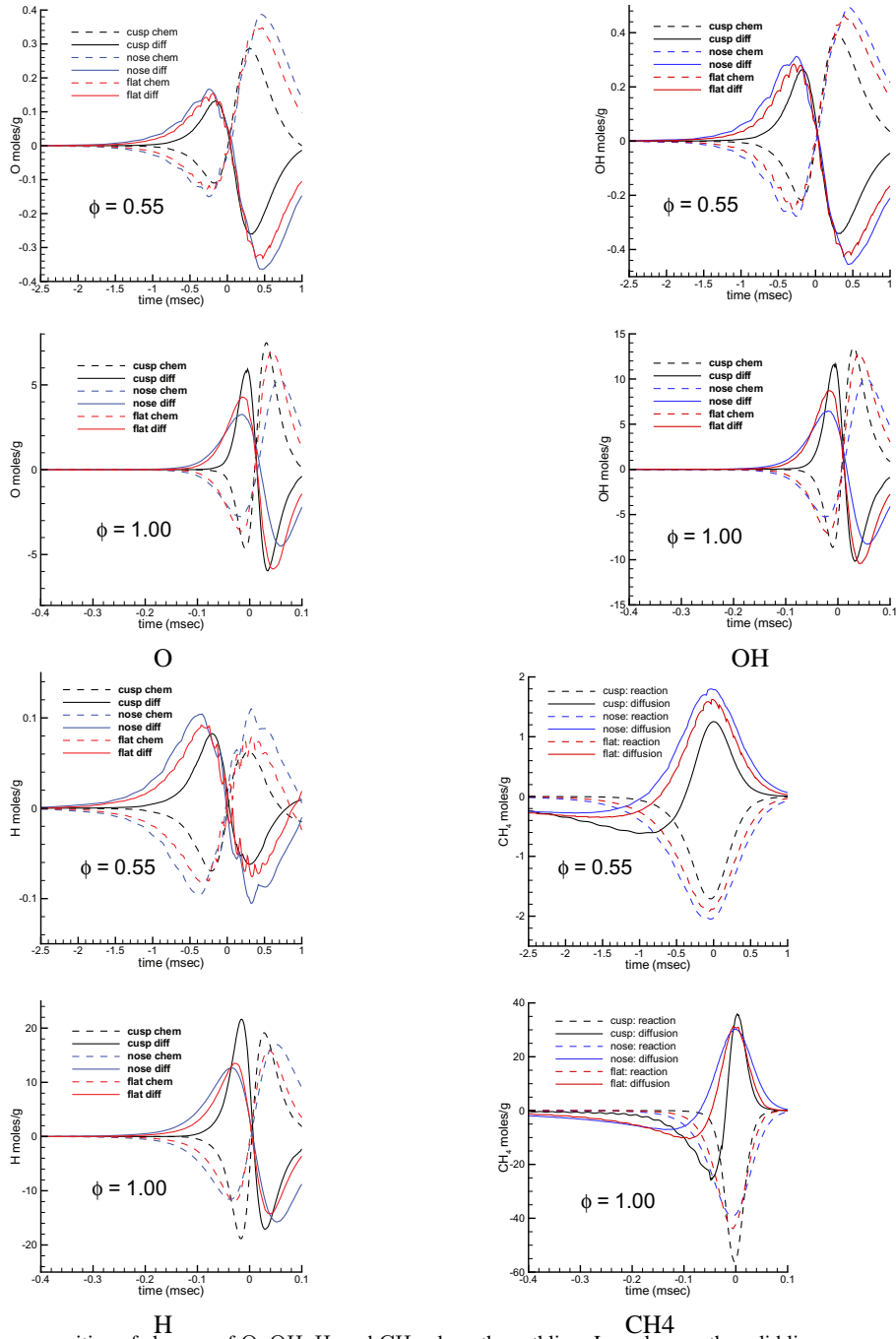
Fig. 5: Decomposition of changes of O, OH, H, and CH_4 along the pathline. In each case, the solid lines represent diffusion and dashed lines represent reactions.